PDO-Related Heat and Temperature Budget Changes in a Model of the North Pacific

JORDAN T. DAWE

Department of Earth and Ocean Sciences, University of British Columbia, Vancouver, British Columbia, Canada

LUANNE THOMPSON

School of Oceanography, University of Washington, Seattle, Washington

(Manuscript received 17 January 2006, in final form 20 June 2006)

ABSTRACT

Heat and temperature budget changes in a ⅓° model of the North Pacific driven by an idealized Pacific decadal oscillation (PDO) atmospheric forcing are diagnosed to determine the roles of atmospheric heat flux and ocean dynamics in upper-ocean heat content and mixed layer temperature (MLT) changes. Changes in MLT and heat content during the transition between negative and positive PDOs are driven primarily by atmospheric heat fluxes, with contributions from ageostrophic advection and entrainment. Once the new PDO state is established, atmospheric heat flux in the central North Pacific works to mitigate the MLT change while vertical entrainment and ageostrophic advection act to enhance it. Upper-ocean heat content is affected in a similar matter, except that vertical processes are not important in the heat budget balance. At the same time, changes in wind stress curl cause the subtropical gyre to spin up and the subpolar gyre boundary to migrate southward. These circulation changes cause a large increase in the geostrophic advective heat flux in the Kuroshio region. This increase results in more heat flux to the atmosphere, demonstrating an active role for ocean dynamics in the upper-ocean heat budget. Eddy heat flux divergence along the Kuroshio Extension doubles after the transition, due to stronger eddy activity related to increased Kuroshio transport.

1. Introduction

Numerous studies have examined the causes and impact of the basin-scale shift in North Pacific surface temperature and mixed layer depth (MLD) that occurred in 1976 (Venrick et al. 1987; Trenberth 1990; Miller et al. 1994a; Trenberth and Hurrell 1994; Deser et al. 1996; Yasuda and Hanawa 1997; Stephens et al. 2001). After this shift, sea level pressure (SLP) in the Aleutian low become lower, central and western North Pacific SST became cooler, and equatorial and eastern North Pacific SST became warmer. This shift is representative of a long-term pattern of decadal variability that extends over the entire Pacific basin (Minobe 1997; Zhang et al. 1997; Deser et al. 2004). Mantua et al. (1997) named this pattern the Pacific decadal oscillation (PDO) and defined a PDO index as the first EOF of monthly SST variability north of 20°N in the Pacific. The PDO index shows significant correlations with a wide variety of climate indices, including fishery populations (Mantua et al. 1997; Chavez et al. 2003), precipitation (Mantua et al. 1997; Deser et al. 2004; Chan and Zhou 2005), and long-term tree ring climatologies (Biondi et al. 2001). [For a review of the PDO, see Mantua and Hare (2002).]

Recently, Deser et al. (2004) found strong correlations between a variety of Indian and Pacific tropical climate indices and the PDO. Since atmospheric signals tend to radiate away from the Tropics to the midlatitudes, these correlations are strong evidence that the PDO has its dynamical roots in the Tropics. However, Deser et al. remark that this finding does not preclude the midlatitude dynamics from modifying the response of the North Pacific system to the tropical forcing or from modifying the tropical forcing by feeding back through an oceanic or atmospheric bridge (Liu et al. 2002; Wang et al. 2003).

There have been many methods proposed by which the midlatitude ocean could participate in the PDO including passive heat flux integration of random atmo-

Corresponding author address: Jordan T. Dawe, Department of Earth and Ocean Sciences, University of British Columbia, 6339 Stores Road, Vancouver, BC V6T 1Z4, Canada.
E-mail: jdawe@eos.ubc.ca

DOI: 10.1175/JCLI4229.1

spheric variability by the mixed layer that results in long-term SST variability (Frankignoul and Hasselmann 1977; Deser et al. 2003); subducted midlatitude SST anomalies reemerging in the Tropics (Gu and Philander 1997); interactions between subtropical wind stress, the shallow tropical–midlatitude overturning circulation, and tropical SST (Kleeman et al. 1999; McPhaden and Zhang 2002); and variability in the transport of the Kuroshio Extension (Qiu 2003). Latif and Barnett (1994, 1996) suggest a coupled mechanism involving SST changes, the midlatitude westerly winds, and Kuroshio transport. Model studies of these mechanisms have concluded that at least part of the North Pacific climate variability may be attributed to a coupled mode of variability between ocean and atmospheric dynamics (Pierce 2001; Pierce et al. 2001).

Studies of the Kuroshio and the Kuroshio Extension have revealed a dynamic system with strong influence on North Pacific SST and heat content [for a review, see Qiu (2002)]. Analysis of temperature and wind data shows that during the late 1970s, the Kuroshio experienced an ~11.6 Sv ($\mathrm{Sv} \equiv 10^6\ \mathrm{m^3\ s^{-1}}$) transport increase due to changes in the wind stress field over the central North Pacific (Miller et al. 1998; Deser et al.1999). Temperature budget analyses of the Kuroshio Extension have shown that geostrophic current changes have a dominant influence on the SST in the area, both through changes in the current strength causing horizontal heat transport divergence (Qiu 2000; Vivier et al. 2002) and through shifts in the latitude of the Kuroshio Extension and its associated frontal systems (Seager et al. 2001; Nakamura and Kazmin 2003). Though most studies of thermal variability in the Kuroshio system have focused on SST, a recent analysis by Kelly (2004) found that heat content in the top 300 m of the Kuroshio Extension is a better predictor of air–sea heat flux than SST. This result is especially interesting in light of the work by Yulaeva et al. (2001), who found that a prescribed heat flux anomaly in the Kuroshio Extension mixed layer forced an atmospheric model more effectively than a prescribed SST anomaly and produced an atmospheric response similar to the atmospheric patterns associated with the PDO (Mantua and Hare 2002).

Mesoscale eddy activity is another significant source of upper-ocean heat transport variability (Roemmich and Gilson 2001). Changes in mesoscale eddy activity in the Kuroshio Extension have been observed (Qiu 2000), associated with the expansion and contraction of the Extension. Qiu and Chen (2005) used data from TOPEX/Poseidon, the Tropical Rainfall Measuring Mission (TRMM), and the Argo array to calculate eddy heat flux, which showed a significant contribution to heat transport in the Kuroshio Extension. However, data only exists over a 6-yr period, so decadal variability in the eddy field could not be examined. Since most long-term climate models are run at relatively low resolutions that do not allow eddies to form, decadal eddy heat flux variability remains unquantified.

To date, model studies of the oceanic response to the PDO have generally been 10–40 year integrations done at 1°–2° resolution with realistic, monthly varying atmospheric forcing using either the National Centers for Environmental Prediction (NCEP)/European Centre for Medium-Range Weather Forecasts (ECMWF) reanalyses or the da Silva monthly marine surface climatology (Miller et al. 1994b; Xie et al. 2000; Ladd and Thompson 2002). These models are too low resolution to resolve eddies or simulate the Kuroshio well. Models with coarse resolution tend to simulate western boundary currents that separate from the coast north of their true location (Hurlburt et al. 1996). This results in unrealistically deep mixed layers near the boundary current, unrealistically large heat fluxes to the atmosphere (Wilkin et al. 1995), and meridional heat transport biases (Maltrud and McClean 2005). In addition, the realistic forcing used in these simulations makes it difficult to separate the oceanic response to decadal changes in the forcing from the low-frequency oceanic response that results from integration of noisy atmospheric forcing (Frankignoul and Hasselmann 1977). Finally, few studies have conducted a full mixed layer temperature (MLT) budget analysis (Miller et al. 1994b), and even fewer have analyzed the upper-ocean heat content (Kelly 2004), which may be the more important variable to consider when studying the influence of the ocean on the atmosphere over decadal time scales.

In this study, we attempt to focus on the response of the ocean to decadal changes in forcing by studying an idealized representation of the PDO forcing applied to an eddy-permitting isopycnal model. In section 2, we present a description of the model, the applied forcing, and the heat flux calculations performed. In section 3, we examine the changes in MLT, MLD, Kuroshio path, and other physical variables that influence the heat budget. In section 4, we look at spatial changes in the 400-m heat content and MLT budgets, and in section 5, we examine changes in the eddy field. Finally, we discuss our results in section 6.

2. Model description

a. Model domain and dynamics

The model used in this study was the Hallberg Isopycnal Model (HIM; Hallberg 1995; Ladd and Thomp-

son 2002). HIM is a primitive equation isopycnal model with a fully nonlinear equation of state. The model has realistic topography and is coupled to a variable density Oberhuber (1993)type mixed-layer model modified to support multiple dynamic layers. The model was configured with 25 layers, three of which represent the mixed layer. The isopycnal layer densities were chosen to resolve the thermocline, especially the density ranges of the mode waters. Only two layers were used to simulate the abyssal ocean. The model was run at ⅓° resolution over a domain extending from 5°S to 65°N, 110°E to 80°W. Open northern and southern boundaries are simulated using sponge layers that relax layer thickness, theta, and salinity to the Levitus monthly climatology. Horizontal viscosity is simulated using a Smagorinsky biharmonic viscosity (Griffies and Hallberg 2000).

To simulate the vertical shear structure of the Ekman layer better, the mixed layer was split into two dynamic layers and a buffer layer that couples the mixed layer to the internal isopycnals. This modification has little direct impact on the MLT budget, as the vertically integrated horizontal advection is unchanged. However, this modification does alter the strength of surface currents (which affect the bulk formulas used to calculate heat flux and wind stress) and the timing of mixed layer convection.

When model temperature falls below freezing, a thermodynamic ice model comes into effect. Once ice has formed, precipitation adds to ice thickness and there is no evaporation; brine rejection and melt water flux are calculated by assuming that the ice has no salt content. No ice dynamics are included, and wind forcing is transmitted through the ice without modification. The ice model only engages in the Sea of Okhotsk and the Bering Sea.

b. Bulk formulas

Latent and sensible heat fluxes, wind stress, and evaporation are calculated at each time step using bulk formulas (Zeng et al. 1998). These formulas parameterize air–sea fluxes as functions of air temperature, humidity, and wind speed, as well as ocean surface temperature and velocity. In contrast, most previous model studies of Pacific decadal variability have used climatologies for all atmospheric forcing (Miller et al. 1994b; Xie et al. 2000; Ladd and Thompson 2002) with some kind of surface temperature relaxation added to prevent the model from drifting from reality. The bulk formulas remove the need for a temperature restoring term since the formulas can be thought of as a relaxation of MLT to air temperature with a coupling dependant on the wind speed. In addition, bulk formulas allow the air–sea fluxes to vary realistically in response to changes in the ocean state, permitting partial ocean–atmosphere feedbacks to occur.

The atmospheric variables input to the bulk formulas are taken from the da Silva monthly climatology. Owing to the long-term averages used to calculate climatologies and the nonlinearity of the relationship between wind speed and wind stress, using the da Silva monthly wind velocity with the Zeng et al. (1998) bulk algorithm results in wind stress values that can be double the da Silva climatology wind stress. To remedy this problem, the da Silva monthly wind stress was run backwards through the bulk algorithm (detailed in da Silva et al. 1994) to generate artificial monthly wind velocity values that are compatible with da Silva wind stress. These artificial wind velocities were used to drive the model's bulk algorithm that calculates wind stress and latent and sensible heat fluxes. While this change has a large effect on the magnitude of the wind stresses, the effect on the latent and sensible heat fluxes is less since they depend both on wind speed and air–sea temperature difference; the net effect is simply a weaker coupling between the air temperature and the ocean surface temperature.

c. Model forcing

Wind, heat, and freshwater forcing drive this model run. As described in the previous section, latent and sensible heat fluxes, wind stress, and evaporation are calculated using bulk formulas. Longwave and shortwave radiation fluxes are calculated from the da Silva monthly climatology, and precipitation is calculated using a monthly climatology derived from the NCEP reanalysis. In addition, surface salinity is relaxed to monthly climatological salinity values with a 90-day time scale. All climatological fields are spline interpolated at each time step.

Idealized PDO-like anomaly fields were generated for each month of the year by taking covariances between the Mantua et al. (1997) PDO index and each month's da Silva climatology anomalies for the period 1945–93 (Fig. 1). These monthly anomaly fields were added to the mean annual cycle after multiplying each by an idealized PDO index. The surface salinity relaxation, precipitation, and sponge boundary fields were the only forcings that did not have a PDO anomaly applied. The function

$$f(t) = \tanh\left(\frac{2\pi(t - t_{\text{shift}})}{3\text{yr}}\right), \tag{1}$$

where t is the model time, and t_{shift} indicates the center of the transition, was used as the model PDO index.

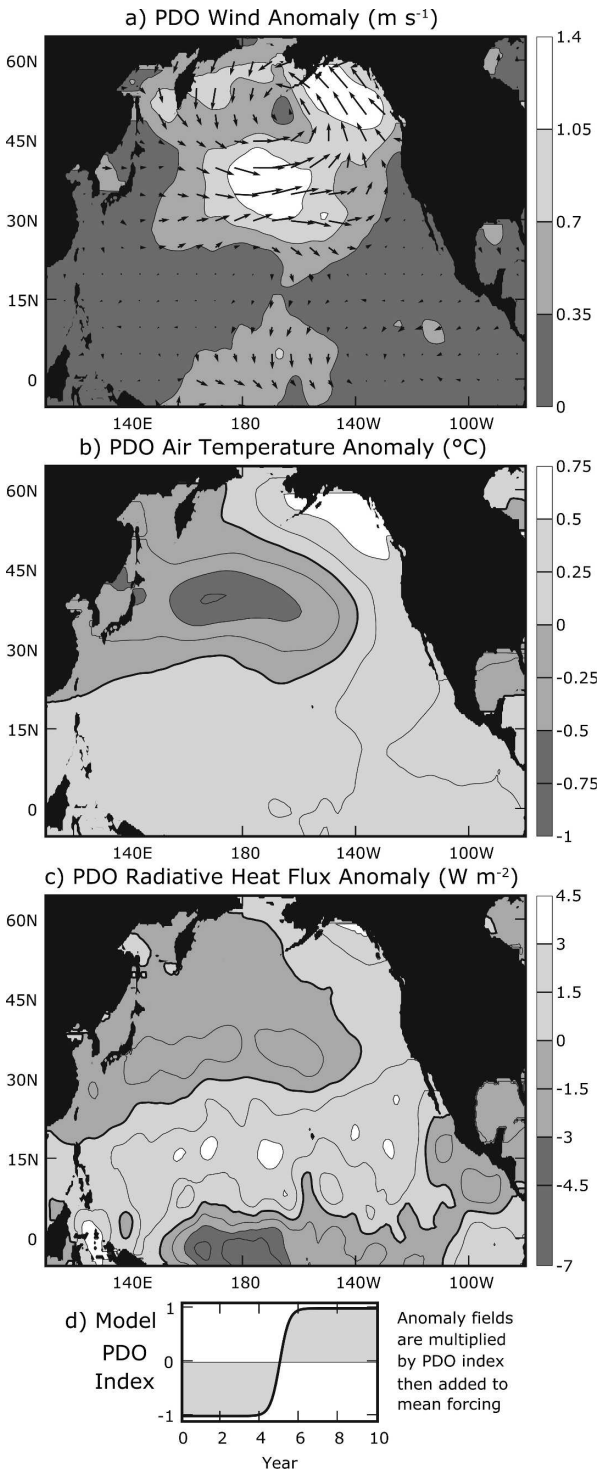

FIG. 1. Idealized PDO forcing: Annual average (a) wind speed anomaly in m s^{-1}; (b) air temperature anomaly in °C; and (c) longwave plus shortwave radiation anomaly in W m^{-2}. Light areas indicate positive anomalies. These anomalies were added to the mean monthly forcing after being multiplied by (d), an idealized PDO index. An anomaly field for specific humidity was also used; specific humidity has a spatial pattern nearly identical to air temperature and therefore is not shown.

This index simulates a rapid negative to positive PDO transition that takes place over two years, like one that occurred in 1976–77.

This idealized forcing was chosen to reduce the effects of observational and atmospheric noise. By taking covariances between the PDO index and the da Silva anomaly data, we hope to construct a more representative picture of long-term decadal variability than would be available from using, for example, the 10 years of anomaly data around the 1976–77 PDO transition. In addition to incorporating more data into our forcing, this smoothing removes most of the interannual noise from the decadal signal, which serves to minimize the ocean's Frankignoul and Hasselmann (1977) response and highlight the ocean's dynamic response. Thus, it is more useful to think of this work as a semi-idealized process study rather than a fully realistic simulation of a PDO transition.

The model was spun up for 45 years in the negative PDO state. The model was then run for 10 years with t_{shift} set to 5 yr, resulting in a transition between negative and positive PDO forcing at the middle of the 10-yr post-spinup period (Fig. 1d). A longer period run after the transition would be desirable, but computational limits and the necessity of a long spinup to equilibrate the system force us to confine our study to the short-term oceanic response. In this paper, we refer to years 1–4 of the run as the negative PDO period, years 7–10 as the positive PDO period, and years 5–6 as the PDO transition period.

The latent and sensible heat flux changes that result from these calculations (Fig. 2a) show a decrease in atmosphere-to-ocean heat transfer of 20–50 W m^{-2} over the Kuroshio along the coast of Asia. The Kuroshio/Oyashio Extension region shows a dipole pattern, with the Kuroshio Extension showing a decrease in atmosphere-to-ocean heat transfer of over 50 W m^{-2}, accompanied by an equally large increase over the Oyashio Extension. Finally, an ~10–20 W m^{-2} increase in atmosphere-to-ocean heat flux occurs in a broad swath over the central North Pacific between 30° and 45°N.

The wind stress changes that result from the model run (Fig. 2b) have nearly the same pattern as the change in the wind velocity. The midlatitude westerly wind stress increases by ~0.05 N m^{-2}. The wind stress curl change, which represents the change in vorticity input to the ocean circulation by the wind, has a dipole structure with intensification of the negative curl over the subtropical gyre and the positive curl over the subpolar gyre. The magnitude of the subpolar wind stress changes are larger than the subtropical, with the maxima occurring near 45°N, 180°.

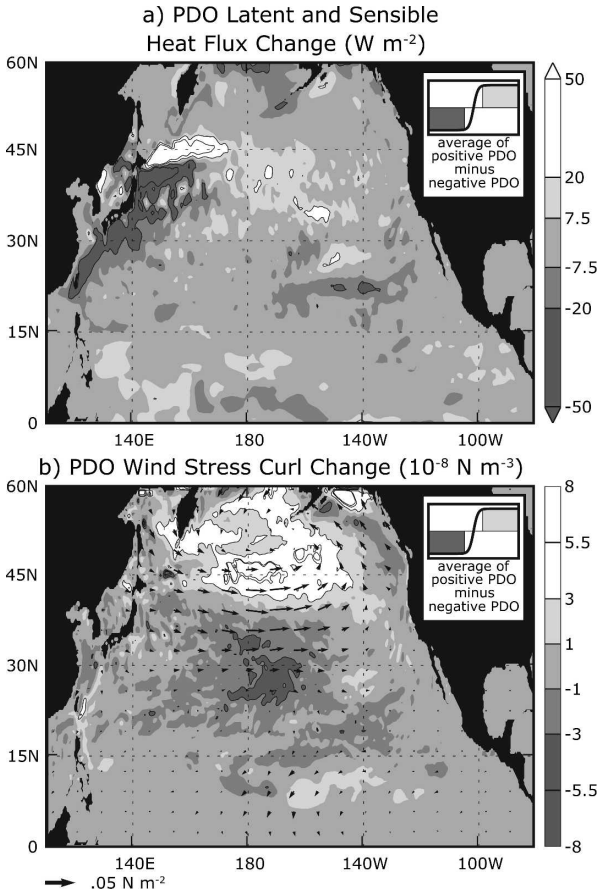

FIG. 2. Model PDO (a) net heat flux (W m^{-2}) and (b) wind stress curl (10^{-8} N m^{-3}) change, calculated as the mean positive PDO state (years 7–10) minus the mean negative PDO state (years 1–4). Light areas in (a) indicate increased flux into the ocean and in (b) indicate increased wind stress curl.

d. *The 400-m heat content and mixed layer temperature budget calculations*

Mixed layer temperature and 400-m heat content budget terms were recorded at each model time step and output as monthly averages. MLT is governed by

$$\frac{\partial T}{\partial t} = -\mathbf{u}\cdot\nabla T - \frac{w_e \Delta T}{h} + \frac{Q}{\rho_0 c_p h} + \kappa\nabla^2 T, \qquad (2)$$

where T is the temperature, $\mathbf{u}$ is the horizontal velocity, w_e is the entrainment velocity at the base of the mixed layer, κ is the eddy diffusivity of heat, Q is the ocean–atmosphere heat flux into the mixed layer, ρ_0 is the mean density of the ocean, c_p is the specific heat of seawater, and h is the depth of the mixed layer.

We calculate the heat content budget over the top 400 m of the ocean to capture all atmospheric fluxes; water deeper than 400 m in the model has no direct contact with the atmosphere. Heat content changes in the upper 400 m of the ocean are given by

$$\rho_0 c_p \int_{-400\text{m}}^{0} \frac{\partial T}{\partial t}\, dz = \rho_0 c_p \int_{-400\text{m}}^{0} -\mathbf{u}\cdot\nabla T\, dz - \rho_0 c_p w T\big|_{-400\text{m}}^{0} + Q + \rho_0 c_p \int_{-400\text{m}}^{0} \kappa\nabla^2 T\, dz, \qquad (3)$$

where w is the vertical velocity.

The model equivalent of (2) and (3) is a complex discretized scheme analogous but not identical to these equations. Therefore, to calculate the terms of these equations we record MLT and 400-m heat content values before and after the relevant model routines, and the difference of these values divided by the model time step is saved. We refer to the five terms of (2) and (3) as the MLT/heat content tendency, the horizontal advection, the entrainment (for MLT)/vertical advection (for heat content), the atmospheric forcing, and the diffusion, respectively. Calculated horizontal and vertical diffusion terms (which averaged ~0.01°C yr^{-1}/~1 W m^{-2}) were much smaller than the advection and atmospheric flux terms (~0.1–10°C yr^{-1}/~5–50 W m^{-2}) and, therefore, have been excluded from our analysis.

Advective fluxes were further decomposed into geostrophic and ageostrophic components. Geostrophic velocities were calculated at each time step within the model code using the Montgomery potential (Montgomery 1937). Within 5° of the equator, where geostrophic balance breaks down, the geostrophic velocities were set to zero. Geostrophic velocities near land points and infinitesimal isopycnal layer thicknesses were also set to zero. These velocities were then run through the model's continuity and tracer advection code to calculate the heat and temperature fluxes caused by the geostrophic flow. Ageostrophic advective fluxes were then calculated by subtracting the geostrophic fluxes from the net advective fluxes.

In our analyses, we make repeated reference to the central Pacific, the Kuroshio Extension, the Oyashio Extension, and the Kuroshio; for clarity, we define these areas in Table 1.

TABLE 1. Defined analysis regions.

Central Pacific	30°–45°N, 170°–150°W
Kuroshio Extension	32°–37°N, 140°E–180°
Oyashio Extension	38°–45°N, 140°E–180°
Kuroshio	Area within 5° of the coast of Asia and Japan from 17° to 35°N

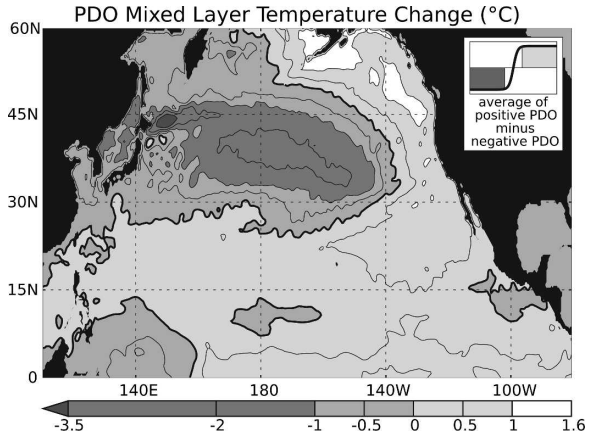

FIG. 3. Model PDO mixed layer temperature change, in °C, calculated as the mean positive (years 7–10) PDO state minus the mean negative (years 1–4) PDO state. Light areas indicate warming.

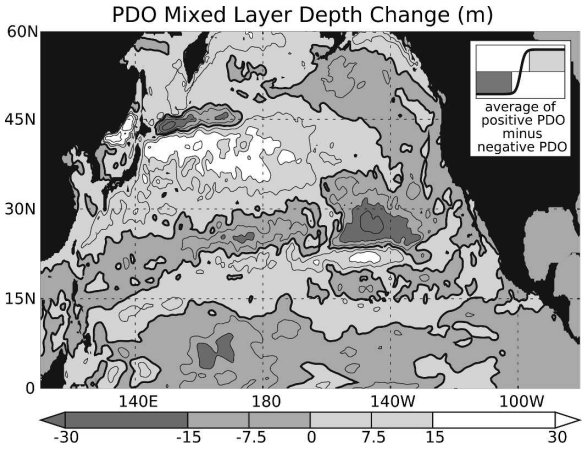

FIG. 4. Model PDO mixed layer depth change, in m, calculated as the mean positive PDO period (years 7–10) minus the mean negative PDO period (years 1–4). Light areas indicate deeper mixed layers.

e. Model Kuroshio

The model shows a bias common to subeddy-resolving models: the Kuroshio separates from the coast several hundred kilometers north of its true position. The model Kuroshio's separation point corresponds with the location of the real-world Oyashio's separation point, which causes part of the Kuroshio transport to join the Oyashio Extension. This northern shift in the separation point causes an excess of heat to be advected up the coast such that the MLT near the separation point is ~10°C too warm. This also causes wintertime MLD in the central North Pacific to be too shallow by ~50 m and wintertime MLD in the Kuroshio Extension to be too deep by ~50 m.

3. Model PDO shift

First, we look at the spatial changes in various model variables, which result from the model PDO shift, to provide a context for the heat budget changes. In this analysis, we take averages over the positive PDO period and subtract the average of the negative PDO period for a variety of model variables.

a. Mixed layer temperature and depth

The MLT difference (Fig. 3) shows good agreement with the PDO regression map generated by the Mantua et al. PDO index (cf. Fig. 2a in Mantua et al. 1997; note that to compare these figures properly, Fig. 3 here must be halved in magnitude), with two exceptions. The first is that the central Pacific in the model cools about twice as much as the observed PDO regression map would indicate; the second is the large 6.5°C cooling in the model's Oyashio Extension.

The pattern of MLD change (Fig. 4) is largely in agreement with the 1976 MLD shift as presented by Deser et al. (cf. Fig. 14 in Deser et al. 1996). The MLD is directly related to the MLT change pattern—warmer MLT means less convection and shallower MLD and colder MLT means deeper MLD. MLD increases in the central Pacific, where the MLT cools, and decreases along the coast of North America, where the MLT warms. There are two exceptions to this direct relationship between MLD and MLT, occurring in the Eastern Subtropical Mode Water (ESTMW: near 25°–30°N, 135°–140°W; Hautala and Roemmich 1998) and the Oyashio Extension. The ESTMW MLD decrease is coincident with a decrease in the magnitude of the wind stress (not shown), resulting in less wind-driven turbulent mixing in the mixed layer; it may also be related to inadequate isopycnal resolution in the ESTMW density range. The Oyashio Extension MLD displays a dipole structure with decreased MLD to the north and increased MLD to the south. This pattern is related to the southward shift of the Oyashio Extension that occurs during the PDO transition, which we discuss in section 3c.

b. The 400-m heat content

The pattern of model 400-m integrated heat content change (Fig. 5) shows significant differences from the MLT pattern. Cooling of the upper ocean in the Oyashio Extension region is more pronounced than in the MLT field (Fig. 3) and extends all the way to the date line. Cooling of the upper ocean north of 25°N

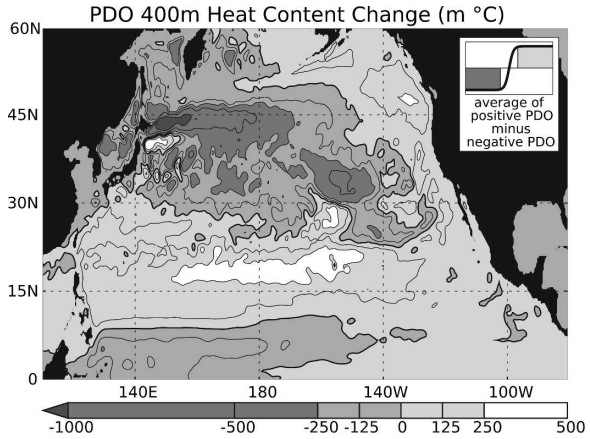

FIG. 5. Model PDO 400-m heat content change, in m °C, calculated as the mean positive PDO period (years 7–10) minus the mean negative PDO period (years 1–4). Light areas indicate warming.

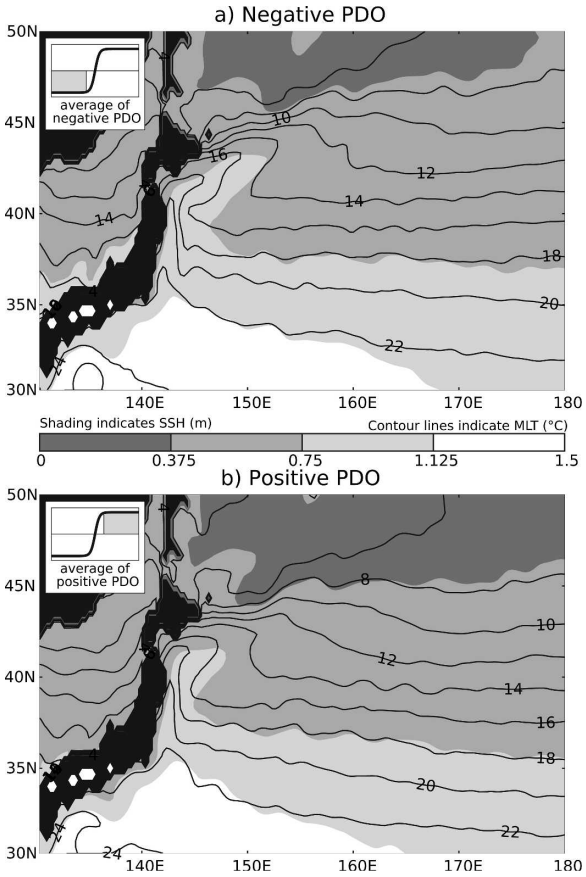

FIG. 6. Mean sea surface height (shading, in m) and mixed layer temperature (contour lines, in °C) for the (a) negative (years 1–4) and (b) positive (years 7–10) PDO periods in the Kuroshio/Oyashio Extension region.

covers a larger area, and the cooling maximum is shifted to the ESTMW area. Finally, there is a prominent warming between 10° and 20°N that is much weaker in the MLT field.

Deser et al. (1999) present a calculation of the 450-m heat content shift between 1970–80 and 1982–90 (Fig. 6 in Deser et al. 1999). The general pattern of heat content changes that they calculate (warmer along the northern, eastern, and southern boundaries of the domain; cooler in the interior) is similar to ours, although details of the pattern differ and the magnitude of our heat content shift is almost double theirs. The main feature of the Deser et al. heat content pattern, a large heating/cooling dipole in the Kuroshio Extension between 30° and 40°N, also appears in the model but is situated farther north in the Oyashio Extension area. This difference is likely due to the northern bias in the separation of the model Kuroshio from the coast of Japan. The similarity of the shifted pattern suggests that the model's Oyashio Extension may be behaving like the real ocean's Kuroshio Extension.

c. Sverdrup response

The strong changes in MLT, MLD, and upper-ocean heat content that occur in the Oyashio Extension can be explained by a southward shift in the geostrophic currents. This southward shift can be seen by comparing the MLT and sea surface height (SSH) fields for the negative and positive PDO periods (Fig. 6). The northern bias of the Kuroshio separation point can be seen in the tongue of high SSH and MLT that extends northward along the coast of Japan. After the PDO transition, the subpolar SSH low expands southward, pushing the coastal tongue of high SSH southward and causing less Kuroshio water to flow into the Oyashio Extension. This diversion of Kuroshio water results in the large cooling in the Oyashio region, as well as the slight warming south of the Oyashio near 40°N (Fig. 3).

To examine the causes of the changes in the Kuroshio/Oyashio current, we evaluate the change in the geostrophic Sverdrup transport, which can be calculated from

$$\psi_g(x) = -\frac{f}{\beta\rho_0}\int_{x_E}^{x} \mathbf{k}\cdot\left(\nabla\times\frac{\boldsymbol{\tau}}{f}\right)dx', \qquad (4)$$

where f is the Coriolis parameter, β is the meridional derivative of the Coriolis parameter, ρ_0 is the mean density of the ocean, $\boldsymbol{\tau}$ is the wind stress, and ψ_g is the integrated geostrophic transport between the surface and the depth where the vertical velocity due to Ekman pumping becomes zero.

The model Sverdrup transport (Fig. 7) shows that both the subtropical and subpolar gyres spin up during the shift. Deser et al. (1999) calculate a peak-to-peak

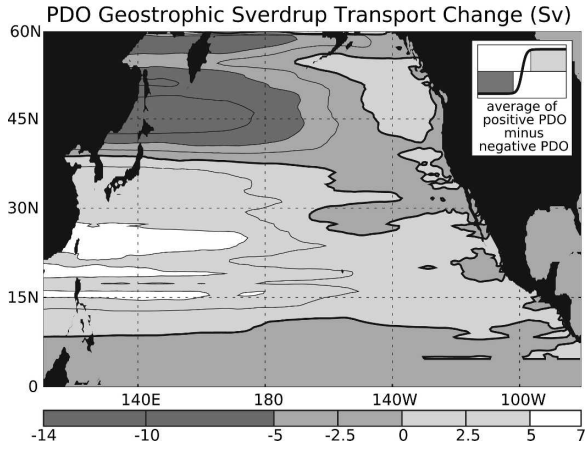

FIG. 7. Model PDO geostrophic Sverdrup transport change, in Sv, calculated as the mean positive PDO state (years 7–10) minus the mean negative PDO state (years 1–4). Light areas indicate increased transport relative to zero at the eastern boundary.

Sverdrup transport change of 11.9 Sv in the Kuroshio Extension during the 1976 climate shift; here, we calculate a 17.3-Sv peak-to-peak change for the Sverdrup transport. Sverdrup transport changes are largest over the position of the Oyashio Extension, suggesting that the Oyashio's southward shift is due to wind forcing.

In summary, the model reproduces the major features of the 1976 PDO shift. The MLT, MLD, heat content, and Sverdrup transport patterns are well simulated, with the exception of the Kuroshio/Oyashio Extension area where the Kuroshio flows too far north. Because of this, the model Oyashio Extension appears to respond to the PDO forcing in a manner similar to the real-world's Kuroshio Extension response. The magnitudes of the changes that the model undergoes are too large by ~50%, possibly due to the back-calculated wind speed climatology used to drive the model, or to the artificial PDO forcing that we used to effect the transition, which removes atmospheric noise forcing that might mask the PDO signal. However, this exaggerated response will be to our advantage as we examine the response of the ocean heat content and MLT budgets to the PDO shift.

4. Spatial patterns in temperature and heat content budgets

a. PDO transition budget calculations

Here we examine the MLT and 400-m heat content budget changes that drive the model's transition from the negative to the positive PDO state. To do this we calculate the average value of each budget term during the PDO transition and subtract the average value of the negative PDO period to generate anomaly fields.

The MLT budget tendency term (Fig. 8a) clearly shows the pattern of the PDO MLT change (Fig. 3). This temperature tendency is forced primarily by the atmospheric term (Fig. 8b), with contributions from the entrainment (Fig. 8c) and ageostrophic advection (Fig. 8d) terms in the central Pacific. The Kuroshio Extension region experiences the largest atmospheric cooling, and here the entrainment and geostrophic advection (Fig. 8e) terms actually work against the temperature tendency. The only region where the atmospheric term opposes the temperature tendency is in a band along 30°N where the cooling is, instead, attributable to the entrainment term. The change in the geostrophic advection shows a great deal of eddy noise but little coherent pattern outside the Kuroshio Extension region.

The 400-m heat content budget tendency term (Fig. 9a) also agrees well with the pattern of PDO heat content differences (Fig. 5). The heat content tendency term is driven primarily by the atmospheric (Fig. 9b) and ageostrophic advection (Fig. 9e) terms north of 30°N, while the vertical advection term (Fig. 9c) dominates south of 30°N. Geostrophic advection (Fig. 9d), as in the MLT budget, shows much eddy noise but few coherent changes outside the Kuroshio, where a strong warming signal occurs, and the Oyashio Extension, where a strong cooling signal appears, due to the southward shift of the currents.

There are two obvious differences between the 400-m heat content and MLT transition budgets. First, the MLT tendency (Fig. 8a) is uniformly negative over the subtropical gyre, while the heat content tendency (Fig. 9a) shows large areas of warming driven by vertical advection. This is most likely the signature of the thermocline deepening in response to Ekman pumping changes. This deepening occurs below the mixed layer and appears not to influence the surface ocean.

Second, the atmospheric heat flux term (Fig. 9b) shows some significant pattern differences compared to the atmospheric MLT budget term (Fig. 8b). The heat flux term has a much greater relative expression in the Kuroshio and Kuroshio Extension regions, compared to the MLT term, due to the deep mixed layers in this region that serve to buffer MLT changes. In addition, the atmospheric heat flux cools the ocean nearly uniformly and does not show the band of warming along 30°N that appears in the atmospheric MLT term. These differences suggest that MLT budgets are not an accurate representation of air–sea heat flux interaction; we will return to this point later.

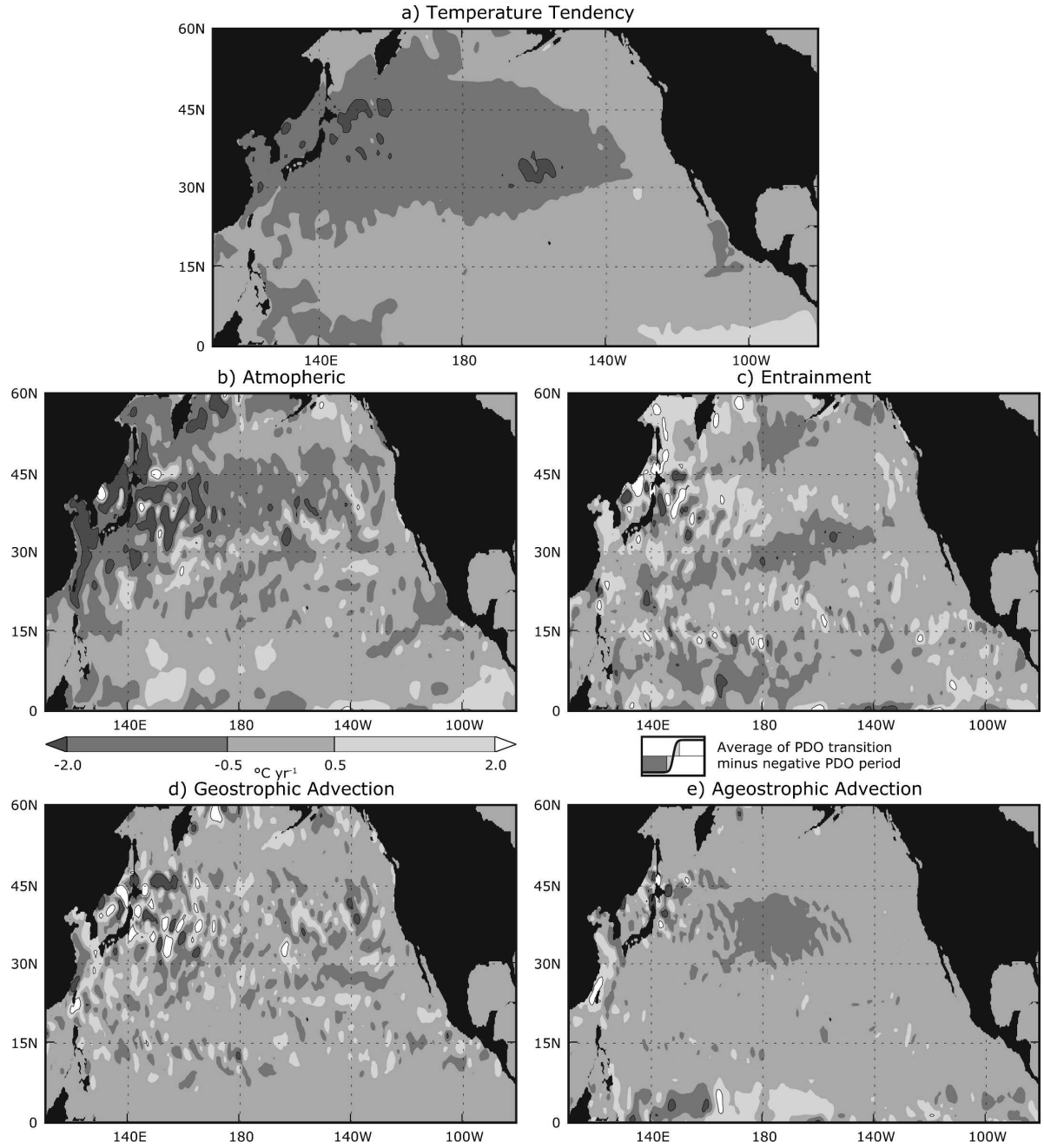

FIG. 8. Mixed layer temperature budget anomalies during the model PDO shift, in °C yr^{-1}. Fields were calculated as the mean PDO transition period (years 5–6) minus the mean negative PDO period (years 1–4); light areas indicate warming. (a) Temperature tendency term, (b) atmospheric term, (c) entrainment term, (d) geostrophic and (e) ageostrophic advective term. A 2° smoothing filter was applied to these fields to suppress eddy noise and improve readability.

b. Positive–negative PDO budget differences

Next, we examine the MLT and 400-m heat content budget differences between the positive and negative PDO periods. To do this we calculate the average value of each budget term during the PDO transition and subtract the average value of the negative PDO period, again generating anomaly fields.

The MLT tendency term (not shown) is nearly zero (~0.1°C yr^{-1}), indicating that the MLT changes occur mostly in the transition period and the MLT has reached approximate steady state. In the central Pa-

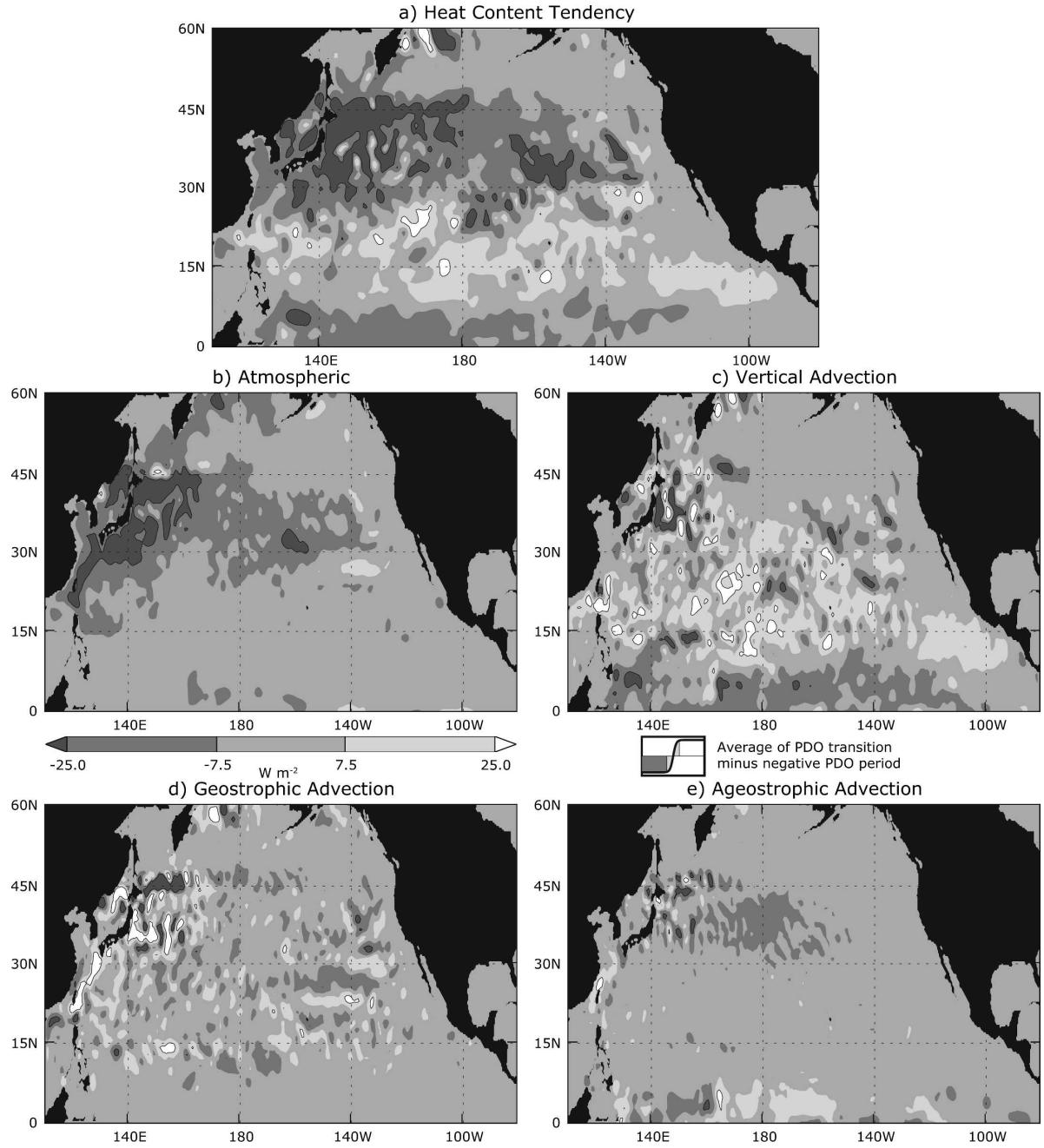

FIG. 9. As in Fig. 8 but for 400-m heat content budget anomalies: (a) Heat content tendency term, (b) atmospheric term; (c)vertical, (d) geostrophic, and (e) ageostrophic advective term.

cific, warming of MLT by the atmospheric term increases significantly after the transition (Fig. 10a), and this increase is balanced by cooling in the entrainment and ageostrophic advection terms (Figs. 10b and 10d). Spatial features of the geostrophic temperature advection change are small scale (~100–200 km) over most of the domain except in the Kuroshio and the Kuroshio/Oyashio Extension system. There, sizeable changes in geostrophic advection and entrainment (Figs. 10b and 10c) are balanced primarily by atmospheric cooling/warming of the opposite sign (Fig. 10a). The changes in the Oyashio Extension show the same dipole pattern that appears in MLT, MLD, and heat content (Figs. 3–5), suggesting that temperature budget changes also result from the southward migration of the Kuroshio separation point.

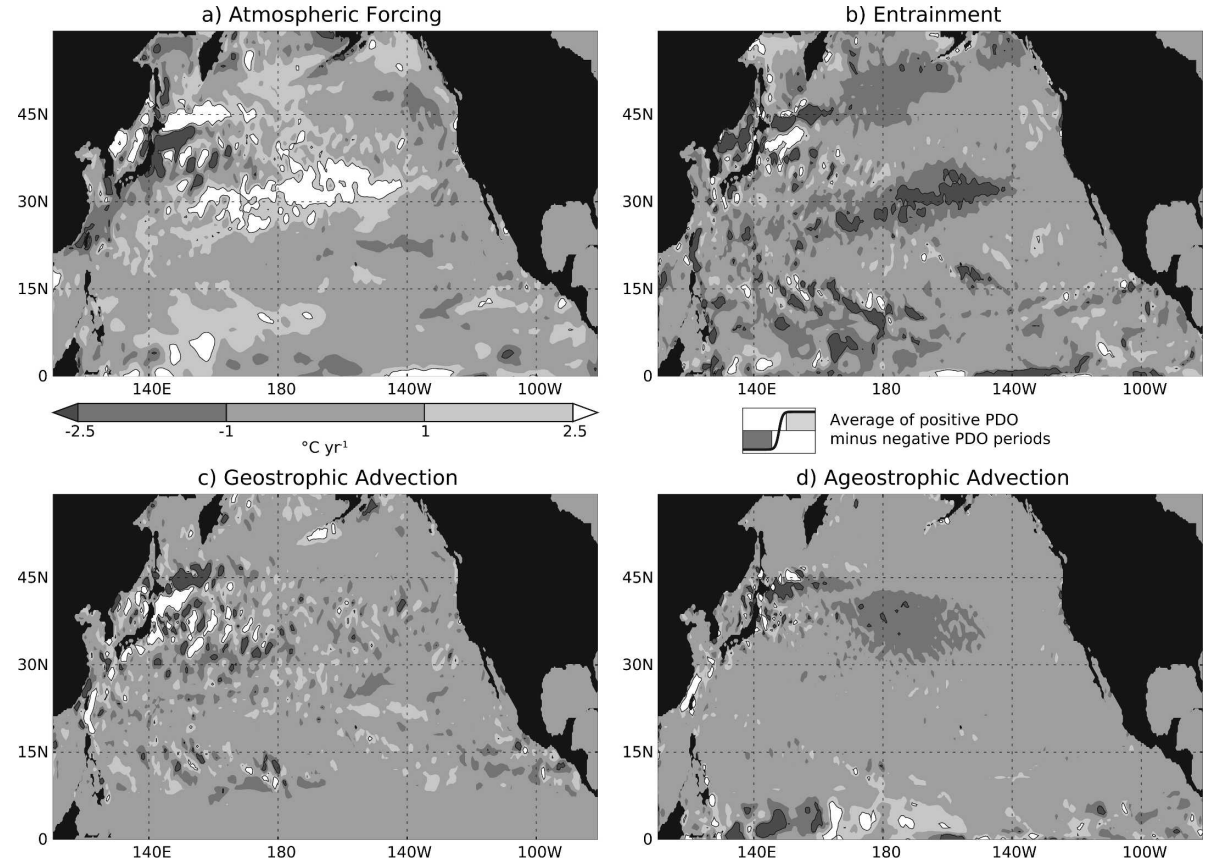

FIG. 10. Model PDO mixed layer temperature budget changes, in °C yr^{-1}. Fields were calculated as the mean positive PDO period (years 7–10) minus the mean negative PDO period (years 1–4); light areas indicate warming. (a) Atmospheric term, (b) entrainment term; (c) horizontal (c) geostrophic and (d) ageostrophic advective term.

In contrast to the quick adjustment in the MLT budget, the heat content budget still shows significant drift in the 4 yr after the shift (Fig. 11e), especially in the Kuroshio/Oyashio Extension. In this region, the horizontal geostrophic (Fig. 11c) and vertical (Fig. 11b) advection terms drive the heat content tendency term, which is consistent with a delayed response caused by Rossby wave adjustment of the gyre circulation.

Geostrophic advection is strongest in the western boundary currents (Fig. 11c). In the Kuroshio and Kuroshio Extension, geostrophic and vertical advection changes combine to produce a 25–50 W m^{-2} warming, balanced by a similar magnitude heat flux to the atmosphere (Fig. 11f). In the Kuroshio, the warming is mostly due to the geostrophic term, but the two terms contribute equally in the Kuroshio Extension. The dipole pattern that appears in MLD and heat content is expressed here as well, with the oceanic advection cooling near 45°N and warming near 40°N; the opposite dipole pattern of warming and cooling appears in flux to the atmosphere. The central Pacific shows a large area of ageostrophic advective cooling (Fig. 11d), which is primarily balanced by the atmospheric term (Fig. 11a) warming the ocean, with additional localized contributions from the vertical and geostrophic advection terms.

Three major points are apparent from examining the MLT and heat content budget changes between the model's negative and positive PDO periods. First, although the atmosphere cools the central Pacific during the model's PDO transition period, once the transition is complete the MLT and heat content budgets both show enhanced warming by the atmosphere. It appears that, once the transition is complete, the additional cooling supplied by ageostrophic advection and entrainment causes the ocean MLT to overshoot the atmospheric temperature change, driving atmosphere to ocean heat transfer. This differs from the observational results found by Yasuda and Hanawa (1997), who found greater central Pacific heat flux from ocean to atmosphere after the 1976 PDO shift. This difference may result from the differing datasets used in our calculations, the lack of atmospheric noise in our forcing, or from the northern bias in our Kuroshio's separation

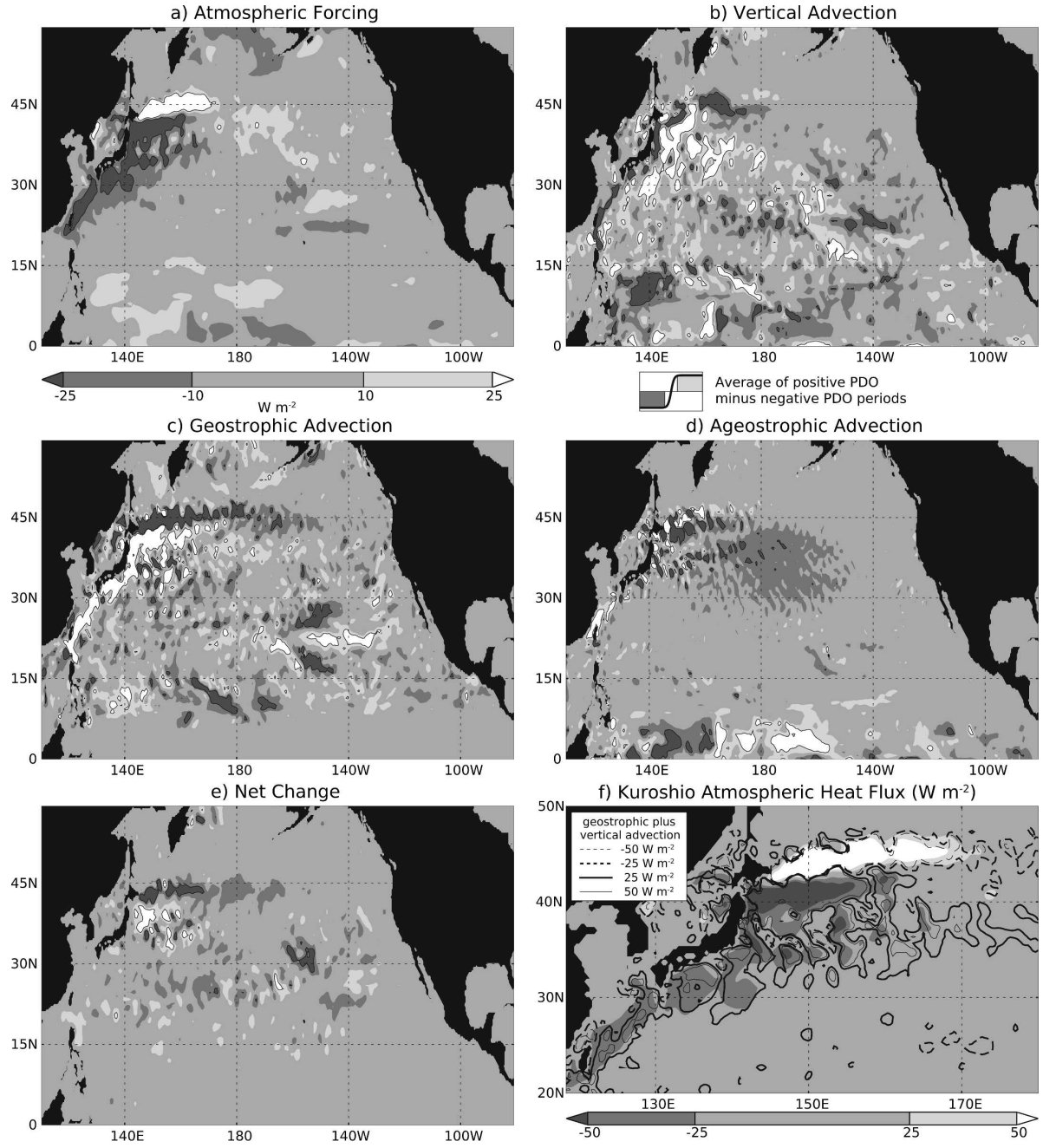

FIG. 11. Model PDO 400-m heat content budget changes, in W m^{-2}. Fields were calculated as the mean positive PDO period (years 7–10) minus the mean negative PDO period (years 1–4); light areas indicate warming. (a) Atmospheric term; (b) vertical, horizontal (c) geostrophic and (d) ageostrophic advective term; and (e) heat content tendency term. (f) An enlargement of the Kuroshio and Kuroshio Extension areas, with shading indicating the atmospheric term changes and contour lines indicating the sum of the geostrophic and vertical advection terms.

position, which reduces the penetration of the Kuroshio Extension into the central Pacific.

Second, there is a strong correspondence between the areas of geostrophic advection and atmospheric heat flux changes over the Kuroshio and especially over the Kuroshio/Oyashio extension dipole (Fig. 11f). The changes in the dipole's heat budget terms exceed 50 W m^{-2}, representing the largest atmospheric heat flux changes in the domain. These changes are no doubt exaggerated due to the northerly bias in the simulation

of the Kuroshio separation point, but they indicate that shifts in the location of temperature fronts, such as observed by Nakamura and Kazmin (2003), have a strong influence on air–sea heat flux. This, along with the increased Sverdrup transport (which brings more warm water into the Kuroshio, consistent with the geostrophic warming), the continuing drift in the heat content budget (of the same sense as the geostrophic advection changes), and the lack of significant atmospheric changes over these current systems (Fig. 1), suggests that the geostrophic heat content advection changes are forcing the changes in atmospheric heat flux.

Finally, there is a striking difference in the pattern and magnitude of the atmospheric term between the MLT and 400-m heat content budgets in the central Pacific. A large atmospheric warming appears in the MLT budget between 30° and 35°N, which is not present in the heat flux field. A similar band of warming appears the in the MLT transition budget. We examine the cause of this discrepancy in the next section.

c. The effect of mixed layer depth

The MLT budget is complicated by the fact that the mixed layer is not a constant body of water—it alters its depth considerably during the PDO shift (Fig. 4). These MLD changes can cause temperature budget changes without any associated heat flux changes, as the same heat flux acts on a greater or lesser amount of water. Here we calculate the impact of changing MLDs on the entrainment and atmospheric temperature budget terms. [As shown in (2), MLD does not affect the advection term.]

Using the atmospheric MLT change term from (2),

$$A = \frac{Q}{\rho_0 c_p h}, \tag{5}$$

the change in A that results due to a change in h of Δh can be written as

$$\Delta A = \frac{Q}{\rho_0 c_p (h + \Delta h)} - \frac{Q}{\rho_0 c_p h} = \frac{-Q\Delta h}{\rho_0 c_p h(h + \Delta h)} = \frac{-A\Delta h}{(h + \Delta h)}. \tag{6}$$

Similarly, for the entrainment MLT change rate E,

$$E = \frac{w_e \Delta T}{h}, \tag{7}$$

we calculate the change in E due to changing h to be

$$\Delta E = \frac{-E\Delta h}{h + \Delta h}. \tag{8}$$

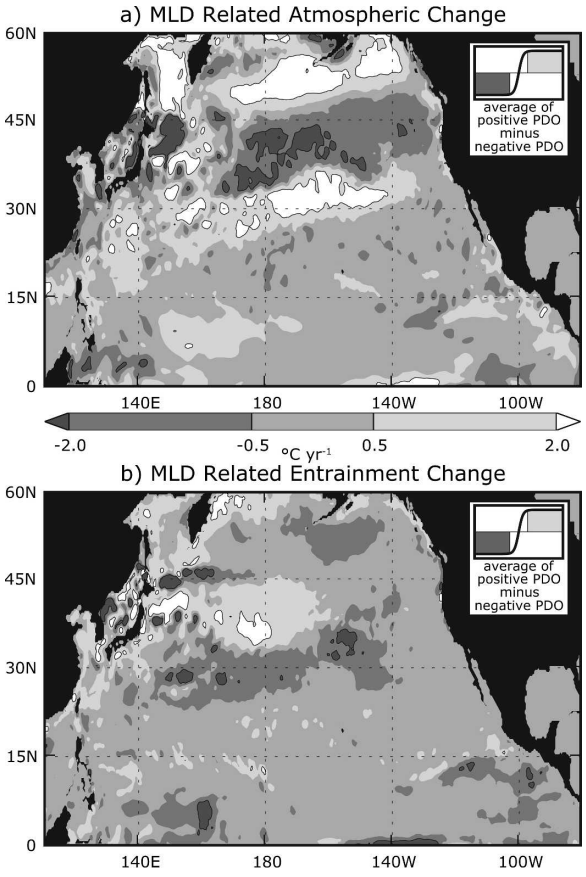

FIG. 12. Model PDO mixed layer temperature budget changes, in °C yr^{-1}, attributable to mixed layer depth changes for (a) the atmospheric and (b) the entrainment temperature budget terms; light areas indicate warming.

The seasonal cycle has a large impact upon MLD, so these calculations were performed by making monthly climatologies of A, E, and h for the positive and negative model PDO periods: Δh was calculated from the monthly differences between the positive and negative PDO period MLD, ΔA and ΔE were then calculated for each month, and the average of all the months was taken.

The results of these calculations (Fig. 12) indeed show that MLD changes have a significant impact on the MLT budget changes. In particular, the band of warming between 30° and 35°N in the MLT budget's atmospheric term is largely the result of MLD changes in that region (Fig. 12a). A similar band of MLD-related cooling also appears in the entrainment term (Fig. 12b). Since midlatitude atmospheric heat flux on average works to warm the mixed layer while entrainment cools it, this pattern of opposing signs in these two terms is a signature of MLD-related MLT budget changes. The large impact MLD can have on the MLT

budget suggests that MLT budgets are poor indicators of decadal heat flux changes.

5. Eddy fluxes

As this model is eddy permitting, eddy heat fluxes can contribute to the heat budget. These fluxes will not be resolved by a lower resolution model, where the smoothness of the temperature and velocity fields precludes the development of anomaly correlations, and may significantly modify the advective budgets in the Kuroshio Extension and other areas with high eddy activity. In this section, we quantify the effects of eddies on the heat flux fields.

Model eddy advective fluxes were calculated by a method analogous to Reynolds decomposition. In our case, we have elected to calculate the eddy flux divergence instead of the flux itself:

$$\overline{u'\frac{\partial T'}{\partial x}} = \overline{u\frac{\partial T}{\partial x}} - \overline{u}\,\overline{\frac{\partial T}{\partial x}}. \tag{9}$$

However, since the model uses a complex discretized algorithm to calculate advection, simply calculating $\overline{u}\,\overline{\partial T/\partial x}$ would not result in the temperature advection calculated by the model. Instead, we use the following analogous scheme. Each month, the model saves mean values for u and T, as well as F, the advective heat flux divergence term. Here F is calculated by saving the upper 400-m heat content before and after the model's advection algorithm and taking the difference. From this saved data, we can calculate the heat flux caused by the model's $\overline{u}$ and $\overline{T}$ fields by feeding them into the model's advection algorithm. Any difference between the mean heat flux saved by the model code and the heat flux divergence calculated using the $\overline{u}$ and $\overline{T}$ fields must be caused by eddy fluxes. In short, we calculate

$$F' = \overline{F} - f(\overline{u}, \overline{T}), \tag{10}$$

where $f(\overline{u}, \overline{T})$ represents the model's heat content advection algorithm.

Since geostrophic eddies have a time scale ~90 days (Gill et al. 1974), using monthly averages would miss much of the eddy activity. However, longer-term averages run the risk of including correlations caused by the seasonal cycle into the eddy fields. To decide what time scale to use, we calculated the eddy flux divergence using both monthly and seasonal averages. Using monthly averages resulted in a smaller eddy flux divergence than using seasonal averages but did not change the spatial patterns appreciably. This lack of change in the spatial patterns leads us to conclude that the seasonal eddy calculation is not biased by the seasonal cycle. Thus, we use the seasonal data in order to include as much eddy variability as possible in our calculations.

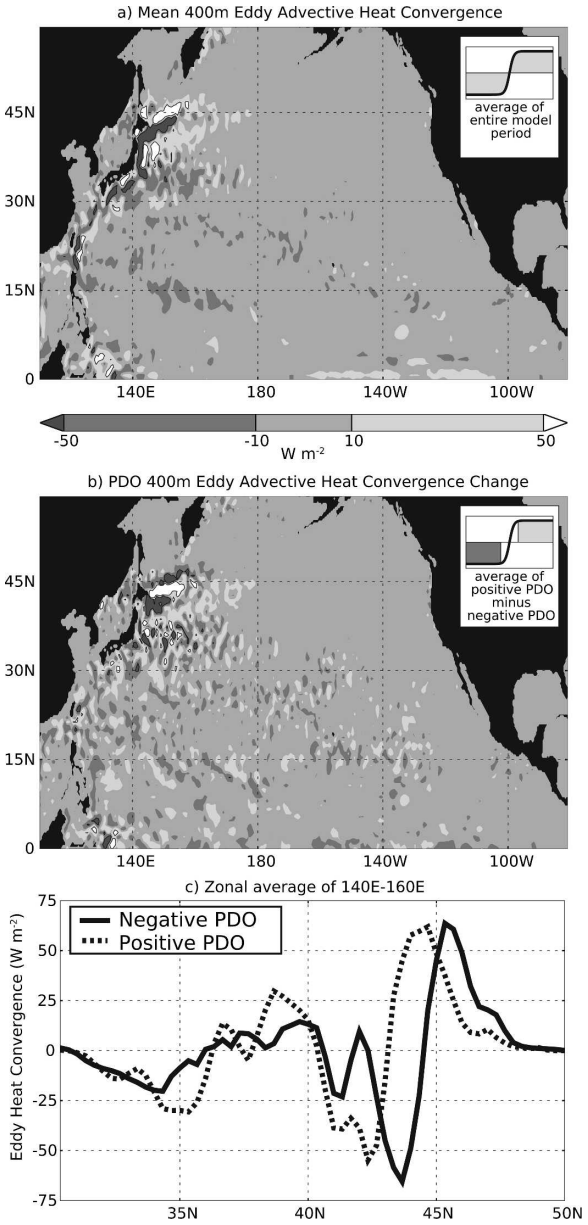

FIG. 13. (a) Mean 400-m eddy heat convergence over the entire model period, in W m^{-2}. (b) Model PDO 400-m eddy heat convergence change, in W m^{-2}, calculated as the mean positive PDO period (years 7–10) minus the mean negative PDO period (years 1–4). Light areas in (a) and (b) indicate warming. (c) Plots of eddy heat convergence in the Kuroshio/Oyashio Extension, zonally averaged from 140° to 160°E. Solid line is the average of the positive PDO period (years 7–10); dotted line is the average of the negative PDO period (years 1–4).

The resulting average flux divergence is large in the Kuroshio, the Kuroshio and Oyashio Extensions, and, to a lesser extent, along the equator (Fig. 13a). The

Kuroshio achieves eddy flux divergence values above 50 W m^{-2}, and the Kuroshio Extension's flux divergences are in the 10–50 W m^{-2} range. The Oyashio Extension shows eddy flux divergences in excess of 100 W m^{-2}, another result of the bias in the Kuroshio separation position. In general, eddy fluxes warm the ocean on the northern side of the boundary currents and cool it on the southern side, working to reduce temperature gradients across the currents.

Taking the differences between the positive and negative PDO periods shows little coherent change in the eddy flux fields outside the Kuroshio/Oyashio Extensions between the negative and positive PDO periods (Fig. 13b). Taking zonal averages from 140° to 160°E in the Kuroshio/Oyashio Extension area over the negative and positive PDO periods clearly shows two different types of eddy response (Fig. 13c). The first type of response appears in the Oyashio Extension near 44°N where the eddy pattern shifts southward by ~150 km without changing magnitude, consistent with a southward shift in the Kuroshio separation point. The second type of response appears in the Kuroshio Extension between 36° and 40°N where the eddy flux divergence doubles in magnitude without an appreciable change in latitude. This is consistent with an increase in eddy activity resulting from stronger Kuroshio Extension transport, causing greater heat flux across the current. Because of the biases in the simulation that reduce the strength of these currents relative to reality, it is probable that the change in the Kuroshio Extension eddy flux in the real ocean would be larger.

6. Discussion

MLT and 400-m heat content budget changes in a model of the North Pacific forced with an idealized PDO-like atmospheric shift were calculated. The pattern of change in the MLT, 400-m heat content, MLD, and Sverdrup transport in the model are in good spatial agreement with observations, but are ~50% too large. The 400-m heat content change pattern shows significant differences from the MLT change pattern, including a much stronger expression in the subtropical gyre. The pattern of MLD change is influenced by wind mixing, thermocline depth, and MLT changes but overall consists of deeper mixed layers where MLT has cooled. Wind stress curl changes alter the transport and separation position of the Kuroshio, which has impacts upon the western pacific MLD, MLT, and thermocline depth. The subpolar gyre experiences twice the Sverdrup transport change that the subtropical gyre experiences, due to the concentration of wind stress changes on the southern edge of the Aleutian low near 45°N.

The shift in model MLT and 400-m heat content that occurs during the transition from negative to positive PDO forcing is forced primarily by atmospheric heat flux, with additional cooling in the central Pacific by entrainment and ageostrophic advection in the MLT budget and ageostrophic advection alone in the 400-m heat content budget. However, once the shift is complete, atmospheric fluxes over the central Pacific begin to warm the ocean in response to continuing cooling by the entrainment and ageostrophic advection terms. MLT budgets settle into the new PDO regime quickly, but the 400-m heat content budget still shows significant drift during the positive PDO period. This may be indicative of a long time-scale dynamic mechanism present in the model that could give rise to decadal variability. We intend to analyze this possibility in a later paper.

Changes in the geostrophic advection appear to control atmospheric heat flux in the western boundary current area in both the MLT and heat content budgets. Increased subtropical gyre transport brings more warm water into the Kuroshio and Kuroshio Extension through changes in the geostrophic and vertical advection terms. In the Oyashio Extension, a cooling/warming dipole appears as the Kuroshio separation point shifts southward. These changes in the geostrophic currents result in increases of heat flux to the atmosphere of ~25–50 W m^{-2} in the Kuroshio Extension and local changes in excess of 50 W m^{-2} in the Oyashio Extension.

The mean eddy field has a large effect on the heat budget in the Kuroshio, Kuroshio Extension, and Oyashio Extension regions, as well as a smaller expression along the eastern equator. Eddy flux divergence shows little organized difference between the negative and positive PDO periods, except in the Kuroshio Extension where the eddy flux across the current roughly doubles. Since eddy activity in the real Kuroshio Extension is likely much stronger than in the model, it appears that eddy fluxes have a localized but possibly significant effect in the Kuroshio Extension during the PDO shift.

The central Pacific pattern of initial cooling by the atmospheric term, followed by warming as the MLT cooling overshoots the atmospheric temperature change, may explain the results of Bond and Harrison (2000), who observed atmospheric damping of anomalous SST during periods when the PDO index is significantly different from zero. If this is the case, it suggests that atmospheric heat flux changes may be strongly dependent on the details of mixed layer dynamics. However, it could equally be the case that this is the result of our specification of atmospheric conditions, which

precludes atmospheric adjustment to changes in the ocean state.

MLT budgets, while capable of explaining the processes that control MLT, can be deceptive when used to examine climate-scale air–sea interactions. MLD changes can strongly alter the MLT budget terms without any changes in the corresponding heat content budget terms. For example, the central Pacific MLT budget period differences shows a strong increase in warming by the atmospheric term near 30°–35°N (Fig. 10a), even though the atmospheric heat content budget term in this area (Fig. 11a) is neutral. On the other hand, vertical advection of isopycnals can alter upper-ocean heat content without affecting MLT, so finding an appropriate depth over which to integrate heat content to cleanly separate these effects is important. Another possible approach would be to calculate heat content changes using a spatially varying depth that is slightly greater than the maximum local mixed layer depth.

The changes that occur in the Kuroshio and the Kuroshio/Oyashio Extension indicate that anomalous geostrophic advection of heat, caused by both transport increases and shifts in frontal locations, strongly impacts atmospheric heat flux in the model's western boundary current region on the decadal time scale. While we have not directly looked at the time evolution of the Kuroshio/Oyashio atmospheric heat flux, the Sverdrup dynamics that drive the geostrophic changes and the continuing heat content adjustment in the years after the PDO transition (Fig. 11e) suggest that the atmospheric heat flux in this area continues adjustment for several years after the shift. This indicates the potential for a large delayed ocean–atmosphere feedback in the Kuroshio/Oyashio Extension in response to changes in central Pacific wind stress curl.

Yulaeva et al. (2001) have attempted to address the question of the impact of oceanic heat flux forcing on the atmosphere and found that a 20 W m^{-2} anomalous heat flux in the Kuroshio Extension results in a decrease in the midlatitude westerlies, causing a reduction of Sverdrup transport in the Kuroshio Extension of 10 Sv. Thus, all of the pieces necessary for a Latif and Barnett (1996)-type ocean–atmosphere coupling in the midlatitude North Pacific have been demonstrated. The missing part of this picture is how strong this type of response is in the real ocean–atmosphere system.

Acknowledgments. We wish to thank Susan Hautala, Neil Banas, and Amanda Babson for helpful comments on an earlier draft of the manuscript, two anonymous reviewers whose comments improved the manuscript significantly, and David Darr, for technical help in the construction of the computational cluster used to perform the model run. Figures were produced using the matplotlib package in the Python programming language. This work was supported by NASA through the Ocean Vector Winds Science Team, JPL Contract 1216233, and the Ocean Surface Topography Science Team, JPL Contract 1267196.

REFERENCES

Biondi, F., A. Gershunov, and D. R. Cayan, 2001: North Pacific decadal climate variability since 1661. *J. Climate,* **14,** 5–10.

Bond, N. A., and D. E. Harrison, 2000: The Pacific Decadal Oscillation, air-sea interaction and central North Pacific winter atmospheric regimes. *Geophys. Res. Lett.,* **27,** 731–734.

Chan, J. C. L., and W. Zhou, 2005: PDO, ENSO and the early summer monsoon rainfall over south China. *Geophys. Res. Lett.,* **32,** L08810, doi:10.1029/2004GL022015

Chavez, F. P., J. Ryan, S. E. Lluch-Cota, and C. M. Ñiquen, 2003: From anchovies to sardines and back: Multidecadal change in the Pacific Ocean. *Science,* **299,** 217–221.

da Silva, A. M., C. C. Young, and S. Levitus, 1994: *Algorithms and Procedures.* Vol. 1, *Atlas of Surface Marine Data 1994,* NOAA Atlas NESDIS 6, 83 pp.

Deser, C., M. A. Alexander, and M. S. Timlin, 1996: Upper-ocean thermal variations in the North Pacific during 1970–1991. *J. Climate,* **9,** 1840–1855.

——, M. A. Alexander, and M. S. Timlin, 1999: Evidence for a wind-driven intensification of the Kuroshio current extension from the 1970s to the 1980s. *J. Climate,* **12,** 1697–1706.

——, ——, and ——, 2003: Understanding the persistence of sea surface temperature anomalies in midlatitudes. *J. Climate,* **16,** 57–72.

——, A. S. Phillips, and J. W. Hurrel, 2004: Pacific interdecadal climate variability: Linkages between the Tropics and the North Pacific during boreal winter since 1900. *J. Climate,* **17,** 3109–3124.

Frankignoul, C., and K. Hasselmann, 1977: Stochastic climate models. Part 2. Application to sea-surface temperature variability and thermocline variability. *Tellus,* **29,** 289–305.

Gill, A. E., J. S. A. Green, and A. J. Simmons, 1974: Energy partition in the large-scale ocean circulation and the production of mid-ocean eddies. *Deep-Sea Res.,* **21,** 499–508.

Griffies, S. M., and R. W. Hallberg, 2000: Biharmonic friction with a Smagorinsky-like viscosity for use in large-scale eddy-permitting ocean models. *Mon. Wea. Rev.,* **128,** 2935–2946.

Gu, D., and S. G. H. Philander, 1997: Interdecadal climate fluctuations that depend on exchanges between the tropics and extratropics. *Science,* **275,** 805–807.

Hallberg, R., 1995: Some aspects of the circulation in ocean basins with isopycnals intersecting the sloping boundaries. Ph.D. thesis, University of Washington, 244 pp.

Hautala, S. L., and D. H. Roemmich, 1998: Subtropical mode water in the Northeast Pacific Basin. *J. Geophys. Res.,* **103,** 13 055–13 066.

Hurlburt, H. E., A. J. Wallcraft, W. J. Schmitz Jr., P. J. Hogan, and J. Metzger, 1996: Dyamics of the Kuroshio/Oyashio current system using eddy-resolving models of the North Pacific Ocean. *J. Geophys. Res.,* **101,** 941–976.

Kelly, K., 2004: The relationship between oceanic heat transport and surface fluxes in the western North Pacific: 1970–2000. *J. Climate,* **17,** 573–588.

Kleeman, R., J. P. Mc Creary Jr., and B. A. Klinger, 1999: A mechanism for generating ENSO decadal variability. *Geophys. Res. Lett.,* **26,** 1743–1746.

Ladd, C., and L. Thompson, 2002: Decadal variability of North Pacific Central Mode Water. *J. Phys. Oceanogr.,* **32,** 2870–2881.

Latif, M., and T. P. Barnett, 1994: Causes of decadal climate variability over the North Pacific and North America. *Science,* **266,** 634–637.

——, and ——, 1996: Decadal climate variability over the North Pacific and North America: Dynamics and predictability. *J. Climate,* **9,** 2407–2423.

Liu, Z., L. Wu, R. Gallimore, and R. Jacob, 2002: Search for the origins of Pacific decadal climate variability. *Geophys. Res. Lett.,* **29,** 1404, doi:10.1029/2001GL013735.

Maltrud, M. E., and J. L. McClean, 2005: An eddy resolving global 1/10° ocean simulation. *Ocean Modell.,* **8,** 31–54.

Mantua, N. J., and S. R. Hare, 2002: The Pacific Decadal Oscillation. *J. Oceanogr.,* **58,** 35–44.

——, ——, Y. Zhang, J. M. Wallace, and R. C. Francis, 1997: A Pacific interdecadal climate oscillation with impacts on salmon production. *Bull. Amer. Meteor. Soc.,* **78,** 1069–1079.

McPhaden, M. J., and D. Zhang, 2002: Slowdown of the meridional overturning circulation in the upper Pacific Ocean. *Nature,* **415,** 603–608.

Miller, A. J., D. R. Cayan, T. P. Barnett, N. E. Graham, and J. M. Oberhuber, 1994a: The 1976–77 climate shift of the Pacific Ocean. *Oceanography,* **7,** 21–26.

——, ——, ——, ——, and ——, 1994b: Interdecadal variability of the Pacific Ocean: Model response to observed heat flux and wind stress anomalies. *Climate Dyn.,* **9,** 287–302.

——, ——, and W. B. White, 1998: A westward-intensified decadal change in the North Pacific thermocline and gyre-scale circulation. *J. Climate,* **11,** 3112–3127.

Minobe, S., 1997: A 50–70 year climatic oscillation over the North Pacific and North America. *Geophys. Res. Lett.,* **24,** 683–686.

Montgomery, R. B., 1937: A suggested method for representing gradient flow in isentropic surfaces. *Bull. Amer. Meteor. Soc.,* **18,** 210–212.

Nakamura, H., and A. S. Kazmin, 2003: Decadal changes in the North Pacific oceanic frontal zones as revealed in ship and satellite observations. *J. Geophys. Res.,* **108,** 3078, doi:10.1029/1999JC000085.

Oberhuber, J. M., 1993: Simulation of the Atlantic circulation with a coupled sea ice–mixed layer–isopycnal general circulation model. Part I: Model description. *J. Phys. Oceanogr.,* **23,** 808–829.

Pierce, D. W., 2001: Distinguishing coupled ocean-atmosphere interactions from background noise in the North Pacific. *Progress in Oceanography,* Vol. 49, Pergamon, 331–352.

——, T. P. Barnett, N. Schneider, R. Saravanan, D. Dommenget, and M. Latif, 2001: The role of ocean dynamics in producing decadal climate variability in the North Pacific. *Climate Dyn.,* **18,** 51–70.

Qiu, B., 2000: Interannual variability of the Kuroshio Extension system and its impact on the wintertime SST field. *J. Phys. Oceanogr.,* **30,** 1486–1502.

——, 2002: The Kuroshio Extension system: Its large-scale variability and role in the midlatitude ocean–atmosphere interaction. *J. Oceanogr.,* **58,** 57–75.

——, 2003: Kuroshio Extension variability and forcing of the Pacific decadal oscillations: Responses and potential feedback. *J. Phys. Oceanogr.,* **33,** 2465–2482.

——, and S. Chen, 2005: Eddy-induced heat transport in the subtropical North Pacific from Argo, TMI, and altimetry measurements. *J. Phys. Oceanogr.,* **35,** 458–473.

Roemmich, D., and J. Gilson, 2001: Eddy transport of heat and thermocline waters in the North Pacific: A key to interannual/decadal climate variability? *J. Phys. Oceanogr.,* **31,** 675–687.

Seager, R., Y. Kushnir, N. H. Naik, M. A. Cane, and J. Miller, 2001: Wind-driven shifts in the latitude of the Kuroshio–Oyashio Extension and generation of SST anomalies on decadal timescales. *J. Climate,* **14,** 4249–4265.

Stephens, C., S. Levitus, J. Antonov, and T. P. Boyer, 2001: On the Pacific ocean regime shift. *Geophys. Res. Lett.,* **28,** 3721–3724.

Trenberth, K. E., 1990: Recent observed interdecadal climate changes in the Northern Hemisphere. *Bull. Amer. Meteor. Soc.,* **71,** 988–993.

——, and J. W. Hurrell, 1994: Decadal atmosphere-ocean variations in the Pacific. *Climate Dyn.,* **9,** 303–319.

Venrick, E. L., J. A. McGowan, D. R. Cayan, and T. L. Hayward, 1987: Climate and chlorophyll a: Long-term trends in the central north Pacific Ocean. *Science,* **238,** 70–72.

Vivier, F., K. A. Kelly, and L. Thompson, 2002: Heat budget in the Kuroshio Extension region: 1993–99. *J. Phys. Oceanogr.,* **32,** 3436–3454.

Wang, X., F.-F. Jin, and Y. Wang, 2003: A tropical ocean recharge mechanism for climate variability. Part I: Equatorial heat content changes induced by off-equatorial wind. *J. Climate,* **16,** 3585–3598.

Wilkin, J. L., J. V. Mansbridge, and J. S. Godfrey, 1995: Pacific Ocean heat transport at 24°N in a high-resolution global model. *J. Phys. Oceanogr.,* **25,** 2204–2214.

Xie, S.-P., T. Kunitani, A. Kubokawa, M. Nonaka, and S. Hosoda, 2000: Interdecadal thermocline variability in the North Pacific for 1958–97: A GCM simulation. *J. Phys. Oceanogr.,* **30,** 2798–2813.

Yasuda, T., and K. Hanawa, 1997: Decadal changes in the mode waters in the midlatitude North Pacific. *J. Phys. Oceanogr.,* **27,** 858–870.

Yulaeva, E., N. Schneider, D. W. Pierce, and T. P. Barnett, 2001: Modeling of North Pacific climate variability forced by oceanic heat flux anomalies. *J. Climate,* **14,** 4027–4046.

Zeng, X., M. Zhao, and R. E. Dickinson, 1998: Intercomparison of bulk aerodynamic algorithms for the computation of sea surface fluxes using TOGA COARE and TAO data. *J. Climate,* **11,** 2628–2644.

Zhang, Y., J. M. Wallace, and D. S. Battisti, 1997: ENSO-like interdecadal variability: 1900–93. *J. Climate,* **10,** 1004–1020.